Rapid Communications

Subterahertz ferrimagnetic spin-transfer torque oscillator

Ivan Lisenkov,[1,*] Roman Khymyn,[2,3] Johan Åkerman,[2,3] Nian X. Sun,[4] and Boris A. Ivanov[5,6]
[1]*Winchester Technologies LLC, Burlington, Massachusetts 01803, USA*
[2]*Department of Physics, University of Gothenburg, 41296 Gothenburg, Sweden*
[3]*NanOsc AB, 16440 Kista, Sweden*
[4]*Electrical and Computer Engineering Department, Northeastern University, Boston, Massachusetts 02115, USA*
[5]*Institute of Magnetism, NASU and MESU, Kiev 03142, Ukraine*
[6]*National Univeristy of Science and Technology, "MISiS," Moscow, Russian Federation*

(Received 17 April 2019; published 25 September 2019)

A theory of magnetization dynamics in ferrimagnetic materials with antiparallel aligned spin sublattices under the action of spin-transfer torques (STTs) is developed. In contrast with antiferromagnets, the magnetic sublattices in ferrimagnets are formed by different magnetic ions, which results in a symmetry breaking in the dynamic equations for Néel's vector. We demonstrate that this symmetry breaking becomes crucially essential for the THz signal extraction in ferrimagnetic spin-torque oscillators. As an example, we consider magnetization dynamics in GdFeCo layers in spin Hall and nanocontact spin-torque oscillator geometries. We demonstrate that (i) the application of spin current leads to a conical precession of Néel's vector with sub-THz frequencies, (ii) in the spin Hall geometry, the conical precession leads to sub-THz oscillations of the Hall voltage, and (iii) in the nanocontact geometry the Néel's vector precession leads to sub-THz oscillations of the magnetoresistance.

DOI: 10.1103/PhysRevB.100.100409

Introduction. Spin-transfer torques [1] (STTs) are widely used to control and excite magnetization dynamics in ferromagnetic materials (FM). Under certain conditions, the STTs can overcome damping and set the magnetization in a steady-state precession [2–4]. The external magnetic field typically defines the frequency of magnetization precession in FM and experimentally achievable values usually lie in the GHz range [5,6].

The action of STTs is not limited to ferromagnetic materials; STTs can act on any other magnetically ordered materials: antiferromagnets (AFMs) [7,8] and ferrimagnets (FiMs) [9,10]. It has been theoretically predicted that the application of spin current on AFM materials leads to a precessing Néel's vector with THz frequencies [11–16]. However, in AFMs the ions forming the magnetic sublattices are of the same type and located in equivalent crystallographic positions. This symmetry dictates the properties of AFMs, which make the extraction of the THz signal extremely difficult. Since the magnetic sublattices in AFMs are formed by identical atoms, partial conductivities for spin-polarized electrons are equal, and therefore one can expect an absence of the giant magnetoresistance (GMR) in an FM/AFM spin-valve structure [17]. At the same time, since the spin-angular momentum of both sublattices is identical, spin current excites an 180° "flat" rotation of Néel's vector, which does not lead to an AC modulation of the spin Hall magnetoresistance in a spin Hall geometry (see Refs. [14,15] and the discussion below).

In this Rapid Communication, we demonstrate that the use of FiM as active layers in spin-torque oscillators provides a straightforward way of THz signal readout. Our numerical and analytical solutions show that a small spin uncompensation in FiM leads to three significant effects: (i) The frequency of the precession can reach sub-THz frequencies, due to the exchange interaction between the sublattices; (ii) the precession of the Néel's vector becomes conical, instead of a flat rotation, allowing a modulation of the spin Hall magnetoresistance with THz frequencies; and (iii) the difference in partial spin conductivities allows for a THz frequency modulation of the GMR in a FiM-based spin-valve structure. As an example FiM material, we consider GdFeCo and calculate expected generated threshold currents and the magnetoresistance modulation depth.

The magnetization in magnetically ordered materials can be controlled by spin currents, which results from the spin Hall effect [3] or spin-polarized charge current [2]. In the first case [see Fig. 1(a)], a charge current density $\boldsymbol{j} = j_x \mathbb{x}$ runs through a Pt layer. A spin-current density $\boldsymbol{j}_{\rm sh}$, produced via the spin-orbit interaction in Pt, penetrates the FiM layer and creates a torque with the polarization $\boldsymbol{p}$ acting on the magnetic sublattices. As the same time, the precession of the magnetic sublattices generates a spin current $\boldsymbol{j}_{\rm sp}$ in the spin-pumping mechanism. Via the inverse spin Hall effect, this spin current induces an electric field $\boldsymbol{E} = E_z \mathbb{z}$ in the Pt, in the direction perpendicular to the charge current. The induced voltage can be characterized by the Hall resistivity of the bilayer $\rho_\perp = E_z/j_x$.

An alternative scenario is realized in a spin-valve geometry [see Fig. 1(b)]. Here, the spin-polarized charge current is generated in the "fixed" polarizer layer with polarization $\boldsymbol{p}$. Then the spin-polarized current flows into the FiM and creates a spin-transfer torque [1] acting on the magnetization. At the same time the resistivity of the contact depends on the mutual orientation of the magnetization in FiM and the polarizer: $\rho = \rho_0 + \Delta\rho\, \boldsymbol{l} \cdot \boldsymbol{p}$. We note here that in FiM the magnetic

*ivan@lisenkov.com

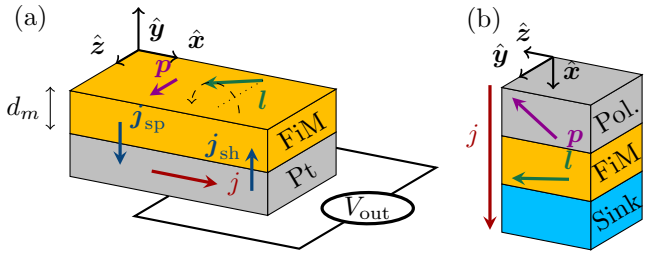

FIG. 1. Sketches showing the geometry of a ferrimagnetic (a) spin Hall oscillator and (b) spin-transfer torque (spin-valve) oscillator. "Pol." stands for polarizer.

sublattices are formed by different magnetic ions, and therefore their partial spin conductivities are different [18].

Besides different physical mechanisms involved in the spin Hall and spin-valve geometries, the magnetic dynamics in both cases can be considered in a unified framework. Magnetization dynamics in FiM is governed by two coupled Landau-Lifshitz equations [19],

$$\hbar\frac{d\boldsymbol{S}_i}{dt}=\left(\boldsymbol{S}_i\times\frac{\delta\mathcal{W}}{\delta\boldsymbol{S}_i}+\frac{1}{S_i}\boldsymbol{S}_i\times\boldsymbol{S}_i\times\boldsymbol{R}_i\right), \tag{1}$$

where $i=1,2$ is the sublattice index, $\boldsymbol{S}_i$ is the effective spin of each sublattice, $\mathcal{W}$ is the free energy per spin of the ferrimagnet, and $\boldsymbol{R}_i$ is the nonconservative term. For uniaxial anisotropy the energy can be written as $\mathcal{W}=\frac{1}{2}\mathcal{W}_{\rm ex}\boldsymbol{S}_1\cdot\boldsymbol{S}_2+\sum_{i=1,2}\mathcal{W}_a(\boldsymbol{S}_i\cdot\boldsymbol{n}_a)^2$, where $\mathcal{W}_{\rm ex}$ is the exchange energy between two sublattices, $\mathcal{W}_a$ is the anisotropy energy, and $\boldsymbol{n}_a$ is an anisotropy axis. The nonconservative term can be written as $\boldsymbol{R}_i=\alpha_{\rm G}\delta\mathcal{W}/\delta\boldsymbol{S}_i-\hbar\sigma j\boldsymbol{p}$. Here, σ is the spin-current polarization efficiency, which depends on the particular spin-current generation mechanism [3,4], j is the charge current density and α_G is the Gilbert damping constant.

Here, we solve the coupled equations (1) both analytically and numerically. For the analytical solution we formulate a σ model, where we substitute the variables $\boldsymbol{S}_i$ with Néel's and total spin vectors: $\boldsymbol{l}=(\boldsymbol{S}_1-\boldsymbol{S}_2)/(S_1+S_2)$ and $\boldsymbol{s}=(\boldsymbol{S}_1+\boldsymbol{S}_2)/(S_1+S_2)$ (see Fig. 2). We also assume that $|\boldsymbol{s}|\ll|\boldsymbol{l}|$, which is true in ferrimagnets with antiferromagnetically ordered but unequal sublattices near a compensation point, i.e., $S_1/S_2\sim 1$. Introducing a spherical coordinate system,

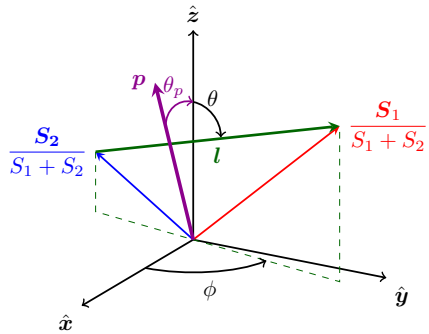

FIG. 2. Schematic representation of Néel's vector $\boldsymbol{l}$ rotation in a ferrimagnetic with uncompensated spins $\boldsymbol{S}_1$ and $\boldsymbol{S}_2$ under spin-transfer torque $\boldsymbol{p}$.

$\boldsymbol{l}=\mathbb{x}\cos\phi\sin\theta+\mathbb{y}\sin\phi\sin\theta+\mathbb{z}\cos\theta$ and $\boldsymbol{p}=p\cos\theta_p\mathbb{z}+\boldsymbol{p}_{\rm IP}$ (see Fig. 2), we can rewrite the dynamical equations in a form [20,21]

$$-\nu\dot\theta\sin\theta+\frac{\dot\theta\dot\phi}{\omega_{\rm ex}}\sin 2\theta+\sin^2\theta\left(\frac{\ddot\phi}{\omega_{\rm ex}}+\alpha_{\rm G}\dot\phi-\tau_z\right)=0, \tag{2a}$$

$$\nu\dot\phi\sin\theta+\frac{\ddot\theta}{\omega_{\rm ex}}+\alpha_{\rm G}\dot\theta-\frac{\sin 2\theta}{2}\left(\frac{\dot\phi^2}{\omega_{\rm ex}}+\omega_a\right)=0, \tag{2b}$$

where the dot stands for a time derivative, $\nu=|(S_1-S_2)/(S_1+S_2)|\ll 1$ is the spin-uncompensation constant, $\hbar\omega_{\rm ex}=\mathcal{W}_{\rm ex}$, $\hbar\omega_a=\mathcal{W}_a$, and $\tau_z=\sigma j\cos\theta_p$. Here, $\omega_a>0$ corresponds to an easy-plane ($\mathbb{x}\mathbb{y}$) and $\omega_a<0$ easy-axis ($\mathbb{z}$) anisotropy. The generalized equations (2) transfer to the σ-model equation for antiferromagnets if $\nu=0$ and to the Landau-Lifshitz equation for ferromagnets, if $S_2\to 0$ and $\omega_{\rm ex}\to\infty$.

A steady solution to this system of equations can be found as $\phi=\omega_r t$, $\cos\theta=\nu\omega_r\omega_{\rm ex}/(\omega_r^2+\omega_a\omega_{\rm ex})$, and $\omega_r=\sigma j\cos\theta_p/\alpha_{\rm G}$. As one can see from this solution, Néel's vector $\boldsymbol{l}$ rotates around the STT direction, as in the AFM case [12,14,15], but for $\nu\neq 0$ the azimuthal angle $\theta\neq\pi/2$, thus Néel's vector never fully lies in the $\mathbb{x},\mathbb{y}$ plane. We can rewrite the relationship between the angle and the rotational frequency in a form

$$\cos\theta=\tilde\nu\frac{\tilde\omega}{\tilde\omega^2+{\rm sgn}(\omega_a)}, \tag{3}$$

where $\tilde\omega=\omega_r/\omega_{\rm afmr}$, $\omega_{\rm afmr}=\sqrt{\omega_{\rm ex}|\omega_a|}$, and $\tilde\nu=\nu\sqrt{\omega_{\rm ex}/|\omega_a|}$ is the effective uncompensation parameter. We note here that $\nu\ll 1$ is the small parameter of the model, however, $\tilde\nu$ can be larger than 1.

Equation (3) is the central analytical result of this work: It connects the precession angle θ with the rotational frequency ω_r. Ultimately, one can calculate the AC resistivities in spin Hall and spin-valve geometries.

Spin Hall geometry. A steady rotation of Néel's vector in the spin Hall geometry (see Fig. 1) generates a spin current $\boldsymbol{j}_{\rm sp}$ via the spin-pumping mechanism [22],

$$\begin{aligned}\boldsymbol{j}_{\rm sp}&=\frac{\hbar g_r}{2\pi}\boldsymbol{l}\times\frac{d\boldsymbol{l}}{dt}\\&=\frac{\hbar g_r}{2\pi}\omega_r[\mathbb{z}\sin^2\theta-\sin\theta\cos\theta(\mathbb{x}+i\mathbb{y})e^{-i\omega_r t}].\end{aligned} \tag{4}$$

Here, we omitted the spin-pumping component coming from the magnetic order [23], because in the case of interest, almost-compensated FiM, the net magnetization is very small comparing to each sublattice magnetization. Using (4) and (3) one can compute the output spin current $\boldsymbol{j}_{\rm sp}$ as a function of the electric current j. The $\mathbb{x}$ component of the spin current $\boldsymbol{j}_{\rm sp}$ generates an AC electric field in the Pt layer across the $\mathbb{z}$ direction via the inverse spin Hall effect (ISHE), $E_{\mathbb{z}}^{\rm AC}=\rho_\perp j e^{-i\omega_r t}=\rho\theta_{\rm SH}\boldsymbol{j}_{\rm sp}\cdot\mathbb{x}e^{-i\omega_r t}$, where ρ is Pt resistivity and $\rho_\perp$ is the Hall resistivity (see Fig. 1), which can be computed as

$$\rho_\perp/\rho=\theta_{\rm SH}\frac{\hbar g_r}{2\pi}\frac{\sigma}{\alpha_{\rm G}}\sin\theta\cos\theta, \tag{5}$$

where $\sigma=\theta_{\rm SH}/(2eS_T d_m)$, e is the elementary charge, S_T is the total volume spin density of all sublattices, d_m is the

magnetic material thickness, and θ_{SH} is the effective spin Hall angle [14,24]. This simple expression does not take into account a finite spin-scattering length in Pt and current shunting through the FiM layer [25,26]. Importantly, the spin-sublattice equivalence in the AFM dictates $\theta = \pi/2$ [15], which results into an absence of AC spin Hall magnetoresistance (5).

Spin-valve geometry. As we mentioned above, the spin-polarized current flowing into the FiM can be scattered predominantly by one species of atoms, which makes the GMR effect possible in FM/FiM structures shown in Fig. 1(b). In this case, the AC part of the longitudinal resistivity can be expressed as

$$\rho_{\parallel}/\rho \approx (\Delta\rho/\rho)\sin\theta\sin\theta_{\mathrm{p}}, \tag{6}$$

where $\Delta\rho$ is spin-valve efficiency. We again note here that due to the inversion symmetry the GMR is not possible in compensated AFMs.

To illustrate the application of our theory we study a spin Hall geometry for a bilayer of Pt and ferrimagnetic GdFeCo. For our calculations we use the following parameters [19,24,27]: $\theta_{SH} = 0.1$, $g_r = 5 \times 10^{18}$ m^{-2}, $\alpha_G = 10^{-2}$, $S_T = M_s/(g_e\mu_B) = 5.4 \times 10^{28}$ m^{-3}, $\omega_{ex}/(2\pi) = 3.34$ THz, $\omega_a/(2\pi) = 12.6$ GHz. The spin-uncompensation parameter in GdFeCo varies with the temperature [27,28] and mutual Gd/FeCo concentrations [29,30]. Especially, GdFeCo can be grown in two configurations, easy plane and easy axis, so here we consider two cases: (i) The easy plane is perpendicular to the interface ($\mathbb{xy}$), and (ii) the easy axis is in the interface plane and along the $\mathbb{z}$ axis.

Easy plane. For a case of an easy-plane anisotropy, the ground state of Néel's vector is $\theta = \pi/2$ and ϕ is arbitrary. An application of STT induces an instability, and Néel's vector starts a rotational motion around the $\mathbb{z}$ axis with the frequency $\omega_r = \sigma j/\alpha_G$. Since we do not consider in-plane anisotropy, this process does not have a current threshold [14].

At the same time, Néel's vector raises above the $\mathbb{xy}$ plane. The dependence of the angle of precession (altitude angle) θ as a function of the rotational frequency ω_r is plotted in Fig. 3(a), calculated using formula (3) and by numerically solving (1). The analytical and numerical solutions demonstrate practically no discrepancy. For small values of STT, $\sigma j < \alpha_G\omega_{afmr}$, the angle of precession approaches zero as the torque increases, since the uncompensated moment tries to align with the torque polarization, and this behavior can be described as FM-like. For large values of torque, $\sigma j > \alpha_G\omega_{afmr}$, the precession angle rebounds and tends back to $\pi/2$ as the value of the torque continues to increase. In this regime, the AFM-like dynamics prevail. Remarkably, that for the small values of $\tilde{\nu}$ the position of the maximum out-of-plane inclination (minimum θ) does not depend on $\tilde{\nu}$, $\omega_r = \omega_{afmr}$. The precession angle reaches a minimum $\theta_{min} = \arccos(\tilde{\nu}/2)$.

If the effective uncompensation constant is large, i.e., $\tilde{\nu} > 2$ (note that ν is still very small), the precession angle can reach the zenith for current densities $j^{th}_{1,ep} < j < j^{th}_{2,ep}$, $j^{th}_{(1,2),ep} = \alpha_G\omega_{afmr}/(2\sigma)(\tilde{\nu} \mp \sqrt{\tilde{\nu}^2 - 4})$. In this situation, all dynamics stops and Néel's vector fully aligns with $\boldsymbol{p}$, similarly to the ferromagnetic case. However, by increasing the values of the STT one can find a point of the AFM-like instability $j^{th}_{2,ep}$ after which the dynamics resumes.

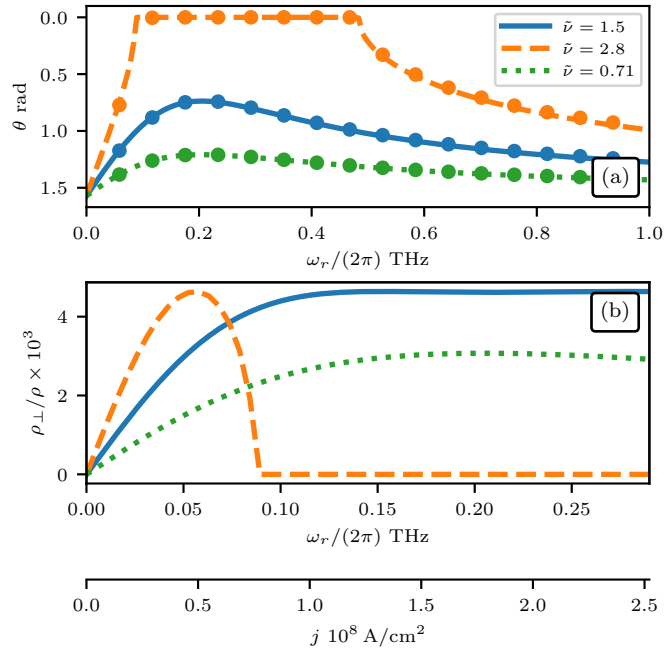

FIG. 3. (a) Altitude angle θ as a function of rotational frequency ω_r for various values of the effective spin-uncompensation parameter $\tilde{\nu}$ for the easy-plane anisotropy. Lines—analytical solution (3); dots—numerical solution of (1). (b) DC to AC Hall resistance as function of the electric current density in the Pt layer and the rotational frequency ω_r.

The induced Hall resistivity is plotted in Fig. 3(b). Formula (5) suggests that the maximum output voltage occurs for $\theta = \pi/4$, thus it is desirable to have $\tilde{\nu} \approx \sqrt{2}$. However, our calculations show that the value of the Hall resistivity is quite robust against varying $\tilde{\nu}$: A decrease of $\tilde{\nu}$ from the "ideal value" leads of a gradual reduction of $\rho_\perp$, although an increase of $\tilde{\nu}$ leads to reducing the bandwidth where the Hall resistance is maximized.

Easy axis. In the easy-axis configuration Néel's vector has two ground states $\theta = 0, \pi$. In a compensated AFM case ($\nu = 0$) these states are fully equivalent. However, the spin uncompensation removes this degeneracy and leads to a different behavior of Néel's vector for opposite directions of the STT. In contrast with the AFM and FM cases, two types of instabilities may exist. One type of instability leads to a FM-like 180° revolution (switching) of Néel's vector from one static equilibrium to another. Another type of instability leads to a steady AFM-like rotation of Néel's vector.

Analyzing (2) we find the thresholds of these instabilities,

$$j^{th}_{\pm} = \frac{\alpha_G\omega_{afmr}}{2\sigma}(\pm\sqrt{4 + \tilde{\nu}^2} + l_z\tilde{\nu}). \tag{7}$$

The dependence of the azimuthal angle for different regimes for the ground state $l_z = -1$ is illustrated in Fig. 4(a). Under a large negative current density $j < j^{th}_-$, Néel's vector experiences an stationary conical precession with angle θ defined by (3). In contrast, if the current density is $j^{th}_+ < j < -j^{th}_-$, Néel's vector switches its ground-state orientation from $l_z = -1$ to $l_z = 1$. Further, if the current density overcomes $j > -j^{th}_-$, Néel's vector starts a precessional motion again.

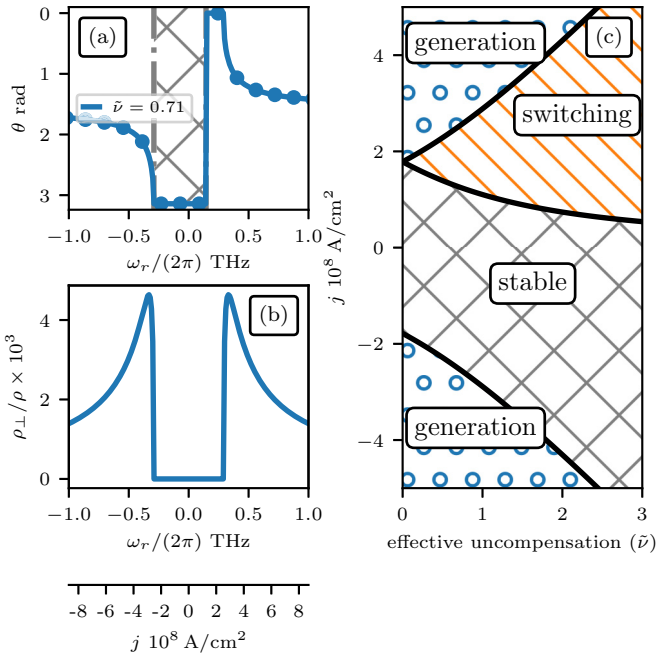

FIG. 4. (a) Equilibrium values of the altitude angle θ as a function of the rotational frequency ω_r for an initial state $l_z = -1$ and the easy-axis anisotropy. Lines—analytical solution; dots—numerical solution of (1). Hatching denotes the region of current densities for which the ground state $l_z = -1$ is stable, calculated from (7). To get the same diagram for $l_z = 1$ one should apply $\omega_r \to -\omega_r$ and $\theta \to \pi - \theta$ (b) DC to AC Hall resistance as function of the electric current density in the Pt layer and the rotational frequency ω_r. (c) Phase diagram of instabilities in an easy-axis ferrimagnet under spin-transfer torques as a function of the spin uncompensation and the current density for the $l_z = -1$ ground state.

The values of threshold current densities strongly depend on the uncompensation constant. The "phase diagram" of the switching and generation instabilities is shown in Fig. 4(c). The spin uncompensation increases the "generation threshold" j_-^{th} and decreases the "switching threshold" j_+^{th}. Therefore, for the generation regime, the FiM should be mostly compensated. However, a small uncompensation is necessary for the conical precession of Néel's vector for a nonzero spin Hall resistance [see Fig. 4(b)]. Thus, for the easy-axis anisotropy, one should choose a compromise between the generation threshold current and the bandwidth of the generation. We also note that for an AFM ($\nu = 0$) the generation threshold equals $|j_\pm^{\text{th}}| = \alpha_G \sigma^{-1} \omega_{\text{afmr}}$, which was found in Refs. [11,15] for an easy-axis AFM.

In conclusion, we developed a theory of ferrimagnetic dynamics under a spin-transfer torque. We demonstrated that the precession of Néel's vector in ferrimagnets is conical and, in contrast with the antiferromagnetic case, this precession generates a nonzero AC spin current. We have shown that in a case of small noncompensation, it is possible to achieve sub-THz frequency precession in a typical GdFeCo ferrimagnetic alloy in both cases of easy-plane and easy-axis anisotropy.

Acknowledgments. B.A.I. gratefully acknowledges support from the National Academy of Sciences of Ukraine via Project No. 1/17 H, Program of NUST "MISiS" (Grant No. K2-2019-006), implemented by the Russian Federation governmental decree dated 16th of March 2013, No. 211; and by the department of Targeted Training of Taras Shevchenko National University of Kyiv at the National Academy of Sciences of Ukraine via project "Elements of ultrafast neuron systems on the basis of antiferromagnetic spintronic nanostructures." R.K. and J.Å. acknowledge support from the Knut and Alice Wallenberg Foundation.

[1] J. Slonczewski, J. Magn. Magn. Mater. **159**, L1 (1996).
[2] S. I. Kiselev, J. C. Sankey, I. N. Krivorotov, N. C. Emley, R. J. Schoelkopf, R. A. Buhrman, and D. C. Ralph, Nature (London) **425**, 380 (2003).
[3] V. E. Demidov, S. Urazhdin, H. Ulrichs, V. Tiberkevich, A. Slavin, D. Baither, G. Schmitz, and S. O. Demokritov, Nat. Mater. **11**, 1028 (2012).
[4] A. Slavin and V. Tiberkevich, IEEE Trans. Magn. **45**, 1875 (2009).
[5] T. Chen, R. K. Dumas, A. Eklund, P. K. Muduli, A. Houshang, A. A. Awad, Dürrenfeld, B. G. Malm, A. Rusu, and J. Åkerman, Proc. IEEE **104**, 1919 (2016).
[6] S. Bonetti, P. Muduli, F. Mancoff, and J. Åkerman, Appl. Phys. Lett. **94**, 102507 (2009).
[7] T. Jungwirth, J. Sinova, A. Manchon, X. Marti, J. Wunderlich, and C. Felser, Nat. Phys. **14**, 200 (2018).
[8] X. Z. Chen, R. Zarzuela, J. Zhang, C. Song, X. F. Zhou, G. Y. Shi, F. Li, H. A. Zhou, W. J. Jiang, F. Pan, and Y. Tserkovnyak, Phys. Rev. Lett. **120**, 207204 (2018).
[9] N. Roschewsky, T. Matsumura, S. Cheema, F. Hellman, T. Kato, S. Iwata, and S. Salahuddin, Appl. Phys. Lett. **109**, 112403 (2016).
[10] T. Okuno, D.-H. Kim, S.-H. Oh, S. K. Kim, Y. Hirata, T. Nishimura, W. S. Ham, Y. Futakawa, H. Yoshikawa, A. Tsukamoto, Y. Tserkovnyak, Y. Shiota, T. Moriyama, K.-J. Kim, K.-J. Lee, and T. Ono, Nature Electronics **2**, 389 (2019).
[11] H. V. Gomonay and V. M. Loktev, Phys. Rev. B **81**, 144427 (2010).
[12] E. V. Gomonay and V. M. Loktev, J. Low Temp. Phys. **40**, 17 (2014).
[13] O. Gomonay, T. Jungwirth, and J. Sinova, Phys. Status Solidi RRL **11**, 1700022 (2017).
[14] R. Khymyn, I. Lisenkov, V. Tiberkevich, B. A. Ivanov, and A. Slavin, Sci. Rep. **7**, 43705 (2017).
[15] R. Cheng, D. Xiao, and A. Brataas, Phys. Rev. Lett. **116**, 207603 (2016).
[16] O. R. Sulymenko, O. V. Prokopenko, V. S. Tiberkevich, A. N. Slavin, B. A. Ivanov, and R. S. Khymyn, Phys. Rev. Appl. **8**, 064007 (2017).
[17] A. H. MacDonald and M. Tsoi, Philos. Trans. R. Soc., A **369**, 3098 (2011).
[18] B. Dai, T. Kato, S. Iwata, and S. Tsunashima, IEEE Trans. Magn. **48**, 3223 (2012).

[19] A. G. Gurevich and G. A. Melkov, *Magnetization Oscillations and Waves* (CRC Press, Boca Raton, FL, 1996).
[20] B. A. Ivanov and A. L. Sukstanski, JETP **57**, 214 (1983).
[21] B. A. Ivanov, Fiz. Nizk. Temp. **45**, 1095 (2019) [in Russian].
[22] Y. Tserkovnyak, A. Brataas, and G. E. W. Bauer, Phys. Rev. Lett. **88**, 117601 (2002).
[23] R. Cheng, J. Xiao, Q. Niu, and A. Brataas, Phys. Rev. Lett. **113**, 057601 (2014).
[24] W. Zhang, W. Han, X. Jiang, S.-H. Yang, and S. S. P. Parkin, Nat. Phys. **11**, 496 (2015).
[25] M. Althammer, S. Meyer, H. Nakayama, M. Schreier, S. Altmannshofer, M. Weiler, H. Huebl, S. Geprägs, M. Opel, R. Gross, D. Meier, C. Klewe, T. Kuschel, J.-M. Schmalhorst, G. Reiss, L. Shen, A. Gupta, Y.-T. Chen, G. E. W. Bauer, E. Saitoh, and S. T. B. Goennenwein, Phys. Rev. B **87**, 224401 (2013).
[26] J. Kim, P. Sheng, S. Takahashi, S. Mitani, and M. Hayashi, Phys. Rev. Lett. **116**, 097201 (2016).
[27] Y. Hirata, D.-H. Kim, T. Okuno, T. Nishimura, D.-Y. Kim, Y. Futakawa, H. Yoshikawa, A. Tsukamoto, K.-J. Kim, S.-B. Choe, and T. Ono, Phys. Rev. B **97**, 220403(R) (2018).
[28] C. D. Stanciu, A. V. Kimel, F. Hansteen, A. Tsukamoto, A. Itoh, A. Kirilyuk, and T. Rasing, Phys. Rev. B **73**, 220402(R) (2006).
[29] T. Kato, K. Nakazawa, R. Komiya, N. Nishizawa, S. Tsunashima, and S. Iwata, IEEE Trans. Magn. **44**, 3380 (2008).
[30] T. A. Ostler, R. F. L. Evans, R. W. Chantrell, U. Atxitia, O. Chubykalo-Fesenko, I. Radu, R. Abrudan, F. Radu, A. Tsukamoto, A. Itoh, A. Kirilyuk, T. Rasing, and A. Kimel, Phys. Rev. B **84**, 024407 (2011).